Batteries & Supercaps

Research Article
doi.org/10.1002/batt.202400691

Chemistry
Europe
European Chemical
Societies Publishing

www.batteries-supercaps.org

Mechanical Properties of Cycled Single Crystal LiNi$_{0.8}$Mn$_{0.1}$Co$_{0.1}$O$_2$ (NMC811) Particles

Ashutosh Jangde,[a, b] Mirtunjay Kumar,[a, b] İdris Tuğrul Gülenç,[a, c] Laura Wheatcroft,[a, b] and Beverley J. Inkson*[a, b]

Single crystal (SC) particle morphologies are attracting significant attention as an alternative to polycrystalline (PC) secondary particles within battery cathodes, to circumvent the degradation paths associated with weak grain boundaries. In the pristine state, the key cathode material LiNi$_{0.8}$Mn$_{0.1}$Co$_{0.1}$O$_2$ (NMC811) exhibits anisotropic mechanical behaviour due to its trigonal $R\bar{3}m$ crystal lattice. Here the mechanical properties of cycled SC NMC811 particles are evaluated in real time using in situ compression in a scanning electron microscope (SEM), as a function of both particle orientation, and electrochemical charge-discharge rate. After 100 cycles, the SC NMC811 particles retain their external morphology, however their non-basal and basal plane fracture strengths systematically decrease as a function of increasing charge rate C/10→2 C, consistent with accelerated lattice degradation. For all charge rates, the cycled and discharged NMC811 single crystal particles retain the $R\bar{3}m$ crystallographic dependence of their strength and deformation mechanisms, with cycled SC particles strongest for compression normal to the (0001) layered structure. The accelerated mechanical softening of cycled NMC811 SC particles at higher C-rates occurs in parallel with degradation of the electrochemical performance of the NMC811 single crystals, and indicates a higher risk of fracture-related degradation processes with fast-charging regimes.

Introduction

Nickel rich LiNi$_{1-x}$(MnCo)$_x$O$_2$ (NMC) layered oxides are key candidates for the next generation of high energy density Li-ion battery cathodes. Most attention has been paid to LiNi$_{0.8}$Mn$_{0.1}$Co$_{0.1}$O$_2$ (NMC811), in particular polycrystalline (PC) NMC811 which typically takes the form of spherical secondary particles consisting of agglomerated NMC primary grains.[1,2] The properties of PC NMC secondary particles are strongly affected by the high density and distribution of their internal grain boundaries, pores and cracks. In particular, grain boundaries between the primary NMC crystallites provide preferential crack paths in pristine, cycled and delithiated PC NMC material.[3–9] Significant intergranular cracking can arise during secondary particle fabrication, occur during electrode processing steps such as mechanical calendering and mixing,[10–12] or occur as a result of internal stresses in NMC secondary particles due to heterogeneous microstructural changes during cycling.[5–7,11] Disrupted Li-ion diffusion paths and accelerated electrolyte-particle corrosion at newly exposed crack surfaces are associated with electrochemical degradation of cycled PC NMC particles.[6,13,14]

Single crystal (SC) NMC has recently been attracting significant attention as an alternative microstructure for cathodes to circumvent the degradation paths associated with weak grain boundaries.[12–17] Single crystal NMC can now be grown with high Ni content, including NMC811,[16,18–23] although the single crystal particle sizes are currently typically in the range 1–5 μm compared to the >10 μm diameters of polycrystalline NMC. The smaller SC particle diameters shorten the Li diffusion path length compared to larger secondary PC particles, although faster Li diffusion may be facilitated in PC particles by grain boundaries and associated cracking.[4,22] Due to their smaller size, more SC particles with a higher particle surface to volume ratio will be required to constitute a given volume of active material compared to larger PC particles. Therefore, depending on the SC size[18] and SC vs PC particle packing efficiencies[12,15,22,23] (which determines overall active material density), SC electrodes may initially have a higher overall volumetric surface area, increasing their susceptibility to surface driven degradation mechanisms. Thus, in optimizing an electrode, there is a complex tradeoff between using potentially fracture resistant but smaller, high surface area single crystal particles, compared to initially reduced surface area, but fracture prone polycrystalline secondary particles.

Due to the micron-level particle sizes of single crystal and polycrystalline NMC it is a challenge to evaluate their mechanical properties. However scanning probe techniques such nano-indentation and in situ probe scanning electron microscopy (SEM) are capable of carrying out mechanical tests on individual

[a] A. Jangde, M. Kumar, İ. Tuğrul Gülenç, L. Wheatcroft, B. J. Inkson
School of Chemical, Materials and Biological Engineering, University of Sheffield, Mappin Street, Sheffield, S1 3JD, United Kingdom
E-mail: beverley.inkson@sheffield.ac.uk

[b] A. Jangde, M. Kumar, L. Wheatcroft, B. J. Inkson
The Faraday Institution, Quad One, Harwell Campus, Didcot, OX11 0RA, United Kingdom

[c] İ. Tuğrul Gülenç
Department of Metallurgical and Materials Engineering, Ankara Yıldırım Beyazıt University, 15 Temmuz Şehitleri Binası – Ayvalı Mah, Halil Sezai Erkut Cad. 150. Sk., Etlik-Keçiören, Ankara, Türkiye

Batteries & Supercaps

Research Article
doi.org/10.1002/batt.202400691

Chemistry Europe
European Chemical
Societies Publishing

particles,[21,24–29] SEM or transmission electron microscopy (TEM) can examine deformation within pillars or sub-micron electron transparent lamellae cut out of particles/grains by gallium focused ion beams (FIB),[19,30–33] and X-ray synchrotron tomography can locate strain gradients and cracks within particles.[34] $R\bar{3}m$ layered oxides intrinsically exhibit both anisotropic elastic constants,[28,35,36] and directional activation of structural defects such as dislocations, slip bands and cracks.[19,24,37] In a recent study, in situ compression of individual pristine single crystal NMC particles has demonstrated that uncycled single crystal NMC811 particles have highly anisotropic behavior under compressive stress,[21] with the activation of non-basal cracking, basal cracking, and (0001) slip dependent on the crystallographic orientation of the particle with respect to the stress field.

In a cathode, the microstructure of a NMC particle, and therefore its mechanical properties, are dependent on a range of factors including its growth method (affecting chemistry, texture, shape and size), electrode and cell processing history (e.g. strain, temperature, electrolyte reactions), and subsequent electrochemical history. Within a rechargeable battery a single crystal NMC particle will oscillate between the Li-rich $R\bar{3}m$ crystal structure of the discharged state, and the Li-deficient charged state. The repeated removal and insertion of substantial Li content has been demonstrated to generate multiple microstructural changes in as-cycled and extracted NMC particles, and in cross-sections of cycled NMC particles cut/ion-milled down to <100 nm thickness for TEM analysis methodologies. NMC811 particle degradation mechanisms reported to date include growth of surface cathode-electrolyte interphase (CEI) layers,[11,38–41] lattice anti-site defects and stoichiometry changes including oxygen, lithium and transition metal (TM) loss,[32,42–46] surface crystalline phase changes to spinel and rock salt structures,[7,42,43,45,47] $R\bar{3}m$ lattice parameter changes, stacking faults, antiphase boundaries, dislocations and slip-bands,[5,19,30,46,48–52] and appearance of internal intragranular cracking associated with chemical/stress gradients.[9,19,22,30–32,34] Importantly, the microstructural changes are not fully reversible with electrochemical charge-discharge cycles, leading to long-term accumulation of residual defects within cycled particles. To date there is limited understanding on how this internal defect accumulation affects the mechanical strength of cycled single crystal NMC particles, and therefore their resilience to deformation, cracking and accelerated surface degradation processes.

In this study we evaluate the quantitative mechanical properties of individual single crystal NMC811 particles, comparing particles in the pristine state to those after extended cycling with a buildup of internal defects. The novel methodology of in situ SEM particle nanoindentation[21,26] is used to directly compress individual NMC811 particles that have been cycled 100 times at three different charge-discharge rates C/10, C/2 and 2 C, and their mechanical properties are evaluated as a function of crystallography and electrochemical history. For each single crystal NMC811 particle, in situ imaging enables the dynamical mechanisms of deformation and fracture to be determined in real time as function of particle morphology and compressive load conditions.

Results and Discussion

NMC811 Single Crystal Particle Microstructure

The pristine commercial NMC811 single crystal particles investigated had sizes predominantly in the 500 nm – 4 µm range (Figure 1). The individual particles were of mixed morphology, being irregular or tabular in shape. As received the particles had an amorphous surface layer, with some variability of thickness in the range 1–10 nm between particles. Tabular single crystals exhibited extended (0001) basal plane facets,[18] with width (in (0001)) to height (along [0001]) aspect ratios of ~1.5–3 (Figure 1). Weakly defined non-basal facets were also apparent on some tabular crystals and smaller more equiaxed polyhedral particles, generally with edges of facets rounded off.
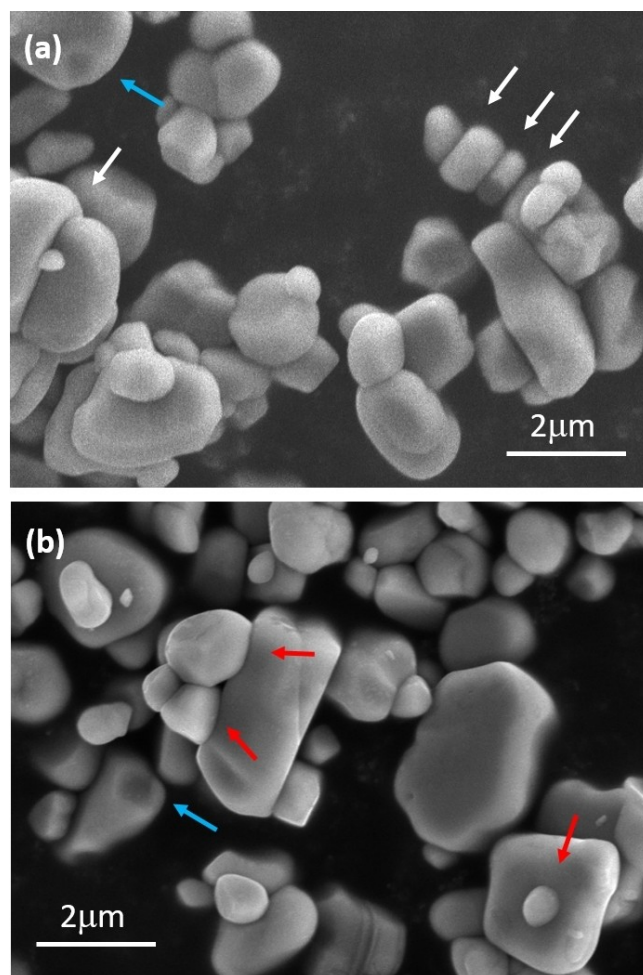

Figure 1. SEM imaging of as received single crystal NMC811 particles. (a) Tabular particles with extended (0001) facets (white arrows) exhibiting frequent oriented alignment of (0001) facets. (b) Concurrent growth of particles attached in small clusters modifies their surface geometry (red arrows). Concave pockmarks were observed on particle surfaces due to cluster detachment (blue arrows).

The tabular NMC811 particles exhibited some oriented alignment of (0001) facets in the as received powder (Figure 1(a), white arrows).

Within the pristine NMC811 material, moderate adherence of the primary single crystals during the growth phase was evident, generating small polycrystalline clusters of 2–5 crystallites. In some cases, adherence during growth caused the primary crystallites to start to grow around each other (e.g. Figure 1(b), red arrows), particularly noticeable with small <1 μm diameter NMC811 particles adhering to larger particles with extended (0001) facets. Some larger 2–3 μm particles exhibited pockmark surface indentations where previously adhered particles had separated, likely during powder processing, leaving residual concave surface impressions (Figure 1, blue arrows).

Electrochemical Cycling of Single Crystal NMC811

The electrochemical cycling behavior of Li-ion battery half-cells using cathodes fabricated from the single crystal NMC811 particles without calendering is shown in Figure 2. When cycled over the voltage ranges of 3.0–4.3 V vs. Li/Li$^+$ at 25 °C, after two formation cycles at C/20 the cell discharge capacity was initially 200 mAhg^{-1} for C/10 charge/discharge rate, 182 mAh g^{-1} for C/2, and 180 mAhg^{-1} for 2 C, comparable to previous single crystal NMC811 particle studies.[16,18,19,22,23] The discharge capacity decreased over 100 cycles dependant on the C-rate used. At C/10 the capacity retention after 100 cycles was 91% (180 mAhg^{-1}). However, at the faster C/2 and 2 C rates after ~50 cycles there was an accelerated capacity loss, and after 100 cycles the capacity retention was down to 59% (108 mAhg^{-1}) at C/2 and 49% (88 mAhg^{-1}) at 2 C respectively. Representative galvanostatic charge and discharge curves for the 1st, 55th and 100th cycles are given in the supporting information (Figure S1).
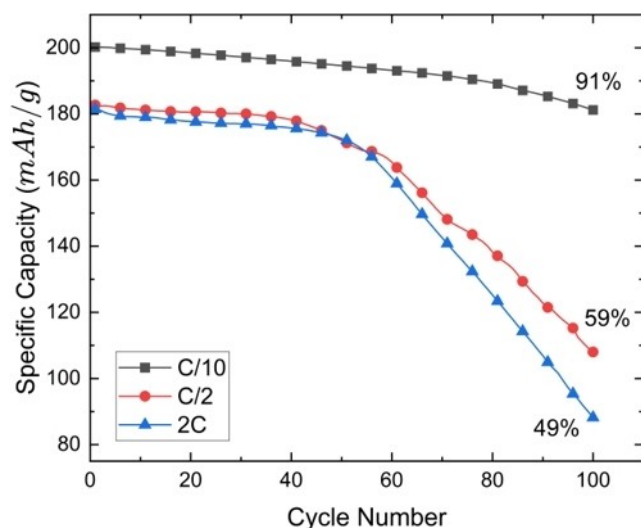

Figure 2. Electrochemical cycling of single crystal NMC811 half-cells. Cell discharge capacity (mAh/g) over 100 cycles 3.0–4.3 V vs. Li/ Li$^+$ at 25 °C, compared for C/10, C/2, and 2 C, with capacity retention after 100 cycles marked.

Cathode Microstructure after Cycling

The microstructures of the NMC811 single crystal cathodes were examined before and after cycling. Before cycling, the NMC811 particles assembled into cathodes exhibited the same features as the pristine powder (Figure 1), being a mixture of individual SC particles and small clusters, with some clusters exhibiting oriented alignment on (0001) facets (Figure 3(a)). Regions of NMC811 particle surfaces had localized adherence of spherical C65 carbon black nanoparticles (Figure 3(e)).

After exposure to electrolyte and electrochemical testing the NMC811 cathodes and cycled NMC811 particles were extracted from the cycled, discharged cells, and their morphology examined by XRD and electron microscopy. Imaging by SEM, there was no significant change in the observed NMC811 particle morphology in situ in the electrodes after cycling for 100 cycles at rates of C/10, C/2 and 2 C (Figure 3), consistent with SC NMC811 cells cycled at or below 4.3 V.[16,19] However, the conductive ~50 nm carbon nanoparticles used in the cathodes (Figure 3(a)) exhibited significant coarsening after electrolyte exposure and cycling, growing to ~100–200 nm domains with a more continuous, interconnected matrix (Figure 3(b–d) inserts, Figure 3(f)). The change in carbon-based matrix morphology increased with the C-rate used, particularly after the C/2 and 2 C charge rates (Figure 3(b–d) inserts and Figure 3(f)). The change in the carbon-based matrix morphology
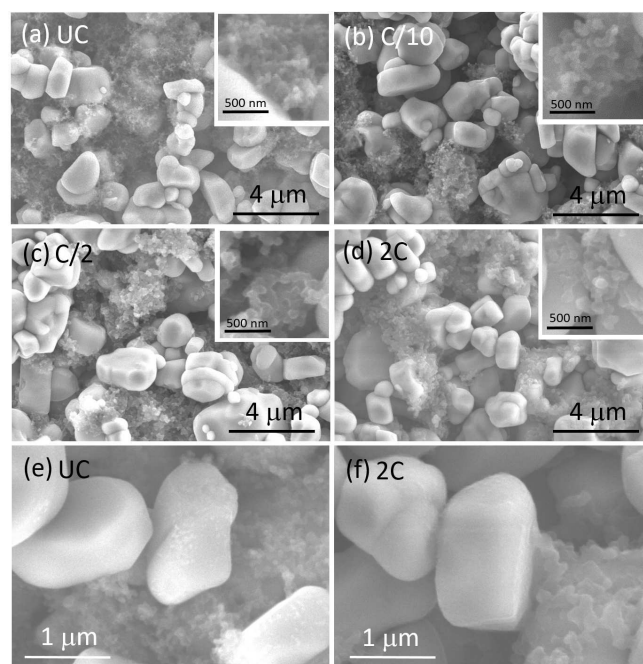

Figure 3. SEM imaging of single crystal NMC811 particle cathodes before and after 100 cycles of 3.0–4.3 V vs. Li/ Li$^+$. (a) As fabricated single crystal electrode with uncycled (UC) NMC811 particles interspersed with 5 wt% PVDF binder and 5 wt% Super C65 carbon black. (b-d) Discharged electrodes after 100 cycles, extraction, rinsing and drying; (b) C/10, (c) C/2 and (d) 2 C. Inserts show the coarsening of conductive carbon morphology between uncycled (a) and 100 cycles (b-d). (e) Fine dispersion of C65 carbon black on uncycled NMC811 particles. (f) Electrode after 100 cycles at 2 C rate exhibiting nanoscale roughness on extracted NMC811 particles, and coarsened, interconnected carbon-based matrix.

Batteries & Supercaps

Research Article
doi.org/10.1002/batt.202400691

Chemistry
Europe

European Chemical
Societies Publishing

is consistent with reaction of the original Super C65 carbon black nanoparticles with electrolyte and dissolved ions, leading to carbon particle swelling, amorphisation and CEI phase formation.[38,53,54]

A mild nanoscale roughening of the NMC811 particles (Figure 3(f)) was also observed by SEM for the faster C/2 and 2 C rate cycled electrodes, in addition to the observed modification of adhered carbon/binder phases. Using TEM, the surface roughness of the 2 C cycled NMC811 particles was associated with growth of an amorphous CEI surface layer, not roughening of the underlying NMC811 crystalline lattice (Figure S2, supporting information). The amorphous layer had variable thickness, predominantly < 15 nm (including any effects of brief specimen air exposure), but thicker in the vicinity of adhered carbon, consistent with concurrent carbon black and NMC811 CEI formation.

Examination of the cycled single crystal NMC811 particles still in situ within the cycled electrodes did not detect any evidence for basal (0001) or non-basal cracking beyond very occasional rough/fracture-like particle facets that were also present in the as received powder due to particle division during powder processing. Similarly, after 100 cycles there was no evidence of residual (0001) slip steps formed by $\mathbf{b} = \frac{a}{3} < 11\overline{2}0 > (0001)$ slip band activation, with the exception of one sub-micron particle extracted from a 2 C electrode identified by TEM to have three 10–25 nm slip steps on parallel (0001) slip planes separated by 40–120 nm (Figure S2a, supporting information). This lack of residual cracking and basal slip in the cycled single crystal NMC811 electrodes indicates resilience to mechanical deformation under the cycling regimes used.

The crystallinity of the single crystal NMC811, both before and after cycling, was characterised by XRD and electron diffraction. XRD confirmed the $R\overline{3}m$ crystal structure of the pristine NMC811, with lattice parameters $a = 2.87$ Å and $c = 14.20$ Å, and $c/a = 4.95$, obtained by Rietveld refinement (Figure S3, supporting information). After cycling, and in a discharged lithiated state, the XRD pattern of the C/10 rate electrode was similar to the uncycled electrode, indicating minimal change in the $R\overline{3}m$ lattice parameters. In contrast, the electrodes cycled at C/2 and 2 C exhibited a reduction in 003, 006, 107 and 018 diffraction peak angles, and an increase in 101, 012, 104, 110 and 113 peak angles (Figure S3, supporting information), consistent with an average increase in the $R\overline{3}m$ c-axis parameter, average decrease in a-axis parameter and increase in c/a ratio. Such NMC811 lattice parameter evolution is typically indicative of Li-loss,[5,48] consistent with the SC NMC811 particles in the C/2 and 2 C rate electrodes exhibiting a degree of remnant delithiation. NMC811 lattice parameter evolution has been linked to modified de-lilthiation/lithiation processes occurring over long term cycling due to CEI growth and surface chemical degradation of NMC811 particles.[7,48] Here, selected area electron diffraction (SAED) examination of SC NMC811 particles extracted after cycling at 2 C-rate showed evidence of surface degradation occurring, specifically localised cubic spinel ordering at the crystalline particle surface,[42,55] producing additional $\{220\}_{spinel}$ diffraction spots down a $[0001]_{NMC}$ direction (Figure S2(c), supporting information).

Mechanical Properties of Uncycled Single Crystal NMC811 Particles

Mechanical compression of the pristine and cycled single crystal NMC811 particles was carried out using the in situ SEM particle mechanical testing methodology previously developed.[21,26] The mechanical behavior of the uncycled single crystal NMC811 particles under compression was consistent with that previously observed for octahedrally facetted SC NMC811 particles.[21] Particles oriented such that the loading axis was < 45 degrees from the (0001) plane typically deformed via basal slip and fracture. Figure 4(a–d) shows an example compression of a 1.0 μm diameter NMC811 single crystal where the propagation of two parallel (0001) basal cracks cleaves the particle into three fragments (Figure 4(b)), with the central ~60 nm thick lamella then undergoing non-basal fracture into multiple fragments (Figure 4(c–d)) as it is crushed further. Rotation of the cleaved particle fragments also helps accommodate the loading asperity (Figure 4(c and d)). The load-displacement curve (Figure 4(e)) shows that the peak load (P_f) sustained by the SC particle was 0.74 mN, with a mean contact pressure (p_m) of 4.2 GPa estimated using the indenter-NMC particle contact radius measured directly from the in situ imaging immediately prior to fracture.

Single crystal NMC811 particles which are compressed with the load axis closer to $[0001]_{R-3m}$ (e.g. perpendicular to the (0001) basal plane) exhibit different mechanical behavior, sustaining much higher loads before non-basal cracking is initiated (Figure 4(g)).[21] Figure 4(h–k) shows the compression of an example tabular SC NMC811 particle, aspect ratio ~3 (2.5 μm width × 0.8 μm thickness) with extended (0001) facets. This particle sustained up to 7.6 mN peak load (P_f), with a mean contact pressure (p_m) of 8.8 GPa, before the initiation of a non-basal crack through the thickness of the particle occurred (Figure 4(i)), associated with a 0.57 mN load drop. This crack opened from < 20 nm to 90 nm width, accompanied by the propagation of a second non-basal crack (Figure 4(j)). These cracks facilitate the generation of a large cleavage fragment, which moves outwards to accommodate the compressing asperity (Figure 4(k)) with an associated 3.6 mN load drop (Figure 4(f)). This particular tabular SC NMC811 particle was only 0.8 μm thick in the [0001] loading direction, and the trans-particle non-basal cracks propagated directly through the whole particle without any visible activation of $\mathbf{b} = \frac{a}{3} < 11\overline{2}0 > (0001)$ type slip.

The pristine NMC811 single crystal particles exhibited strong mechanical anisotropy due to the inherent difficulty of activating non-basal dislocation activity in the $R\overline{3}m$ structure (Figure 4(g)).[21] When loading perpendicular to the (0001) layered structure, secondary basal slip was observed in some single crystal NMC811 particles after activation of primary non-basal cracking, to enable the lateral motion of material to accommodate stress from the compressing asperity (Figure S4, supporting information).[21] Shear bands have also been observed after indentation of ~10 μm grains in polycrystalline sintered NMC811.[28] In the uncycled NMC811 particles here,
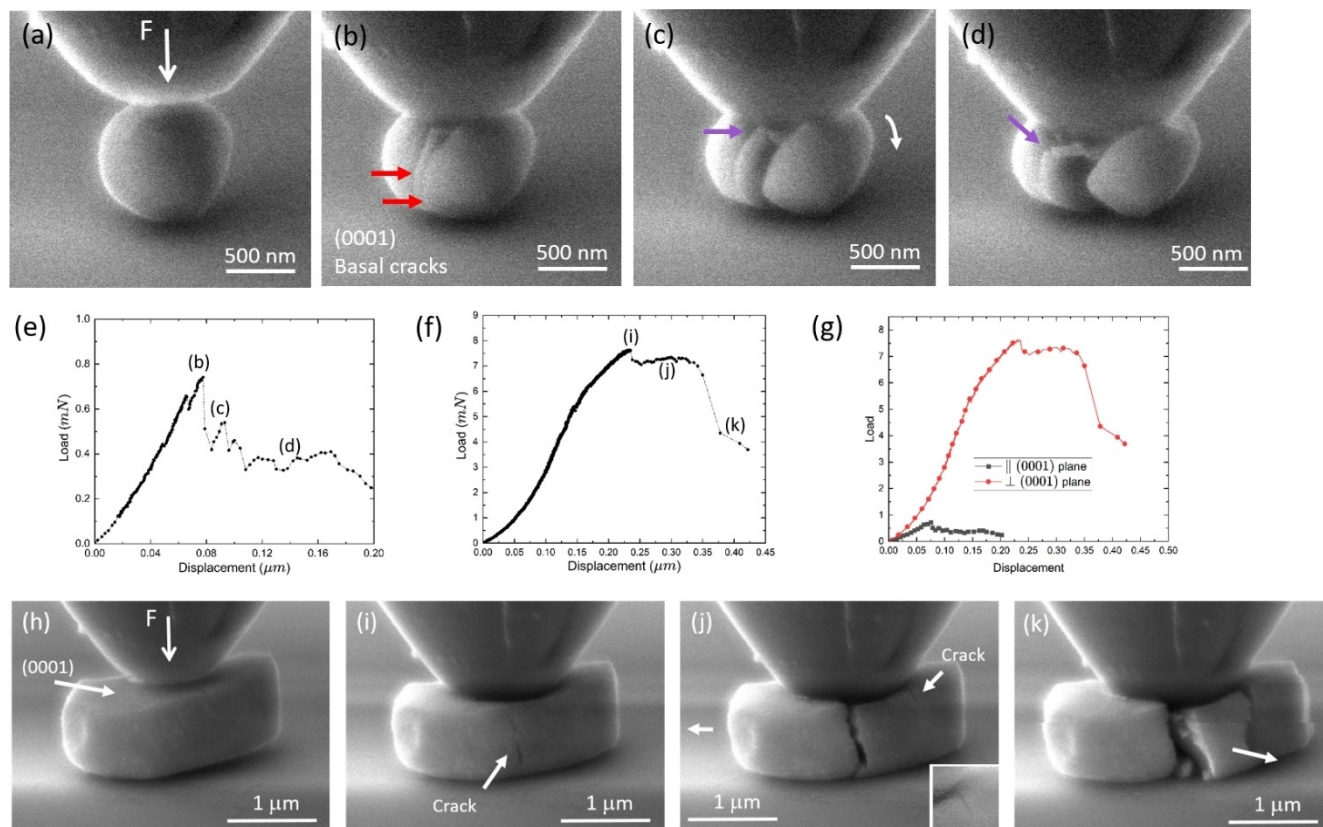
Batteries & Supercaps

Research Article
doi.org/10.1002/batt.202400691

Chemistry
Europe
European Chemical
Societies Publishing

Figure 4. Compression of uncycled single crystal NMC811 particles compressed with a load axis F near parallel (a-d) and perpendicular (h-k) to the $(0001)_{R-3m}$ basal plane. The timings of SEM images are indicated on the corresponding load displacement curves in (e,f). (a-d) 1 μm diameter SC NMC811 particle, (a) prior to load, (b) propagation of two parallel (0001) basal cracks (red arrows) at 0.74 mN peak load generating a 60 nm thick lamella, (c,d) non-basal secondary fractures of (0001) lamella (purple arrows) and rotation of right hand cleavage fragment. (e) Load-displacement curve for (a-d). (f) Load-displacement curve for (h-k). (g) comparison of (e) and (f). (h-k) 2.5 μm diameter tabular NMC811 particle with extended (0001) facets, (h) start of load, (i) propagation of non-basal crack at 7.6 mN peak load, (j) crack opening by movement of left-hand side of particle, and initiation of second non-basal crack (highlighted in insert), (k) crack widening and displacement of cleavage fragment (white arrow).

visible slip steps were only generated on (0001), consistent with the $\mathbf{b} = \frac{a}{3} < 11\bar{2}0 > (0001)$ slip systems.[19,21,50]

Mechanical Properties of Single Crystal NMC811 Particles Cycled at C/10 Charge/Discharge rate

Mechanical compression testing was carried out on single crystal NMC811 particles extracted from the cycled, discharged cells (C/10, C/2 and 2 C rates), using the same in situ test parameters used for the uncycled particles.

After 100 cycles at C/10, the SC NMC811 electrode cells retained 91% of their original capacity (Figure 2(d)). Under in situ compression testing, the discharged C/10 NMC811 particles exhibited deformation mechanisms similar to the uncycled particles, retaining a strong mechanical anisotropy. Depending on the orientation of the (0001) basal planes with respect to the loading axis, particles deformed by basal slip/fracture (e.g. Figure 5(a–c)), or by non-basal fracture combined with secondary basal slip/fracture (Figure 5(d–i)). As for the uncycled NMC811 particles, C/10 single crystal particles with (0001) oriented close to the loading axis failed at the lowest loads. For example, the 2.0 μm diameter C/10 NMC811 particle

in Figure 5(a) sustained a peak load of $P_f = 1.0$ mN, with mean contact pressure p_m of 2.1 GPa, before rapid transparticle propagation of a near-median (0001) crack bisected the particle enabling rotation of the generated fragments (Figure 5(b)). By comparison, the C/10 SC NMC811 particle in Figure 5(d) compressed down [0001] sustained a first peak load P_f of 3.7 mN and mean contact pressure p_m of 7.7 GPa (Figure 5(i)), after which two median non-basal cracks and a lateral (0001) basal crack generated a quadrant-shaped cleavage fragment associated with a 0.9 mN load drop (Figure 5(e)).

The C/10 NMC811 particle in Figure 5(d) was one of the larger single crystals tested at ~3.0 μm diameter, with no major facets and mild surface irregularity/pock-marks. A short MP4 video is available for this test in Supporting Information (MP4-1). Under compression the maximum load sustained by the particle was $P_m = 4.0$ mN, which occurred 0.5 μm deep into the particle, after the rounded surface had first fractured at load $P_f = 3.7$ mN (Figure 5(i)). Continued compression generated multidirectional deformation around the asperity via non-basal and basal fracture, together with secondary activation of $\mathbf{b} = \frac{a}{3} < 11\bar{2}0 > (0001)$ slip systems generating parallel slip bands perpendicular to the [0001] load axis (Figure 5(f–h)). The sequential activation of cycles of non-basal/basal cracking and
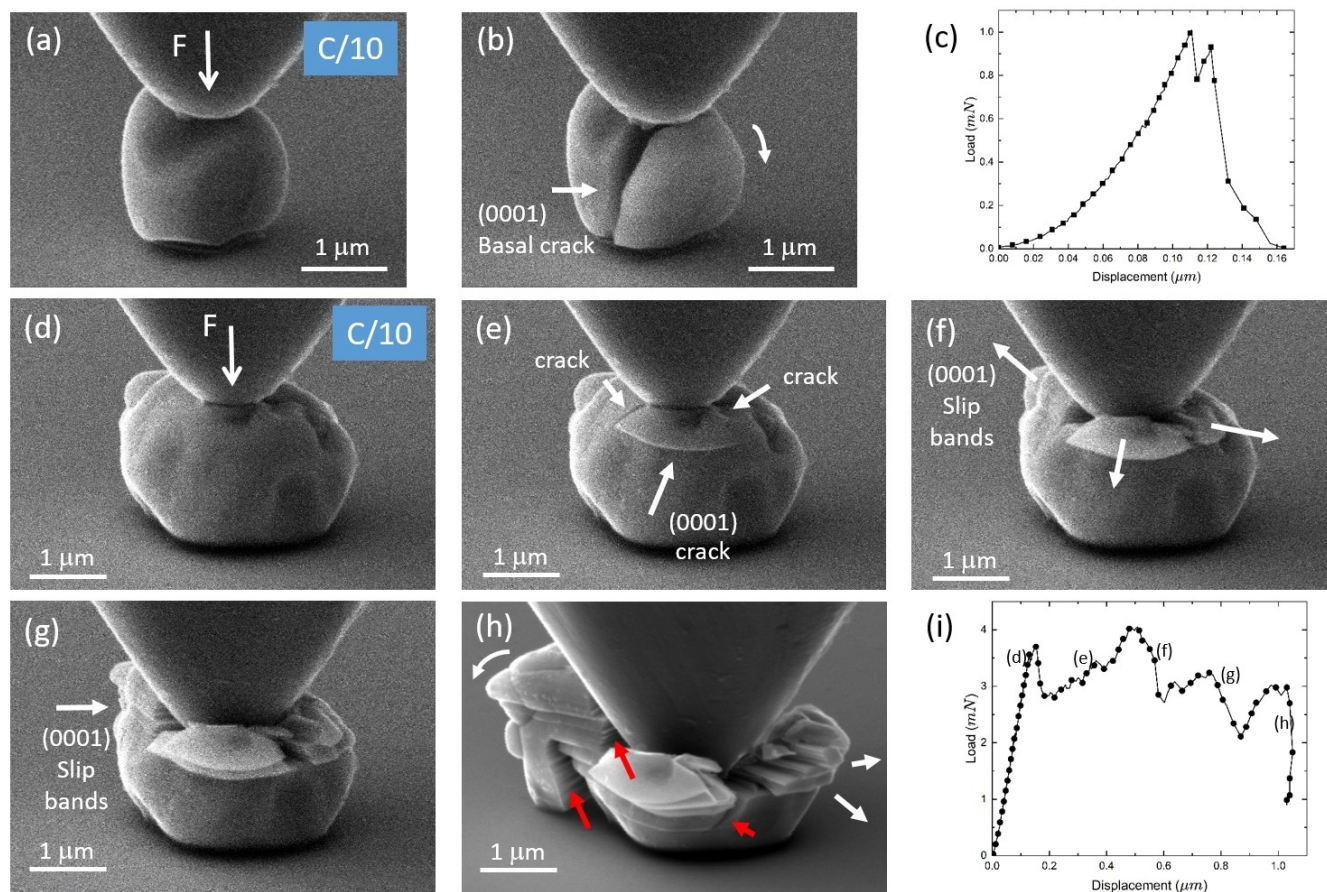
Batteries & Supercaps

Research Article
doi.org/10.1002/batt.202400691

Chemistry Europe
European Chemical
Societies Publishing

Figure 5. Compression of single crystal NMC811 particles after 100 cycles of 3.0–4.3 V vs. Li/ Li⁺ at C/10. (a-c) 2.0 μm diameter particle compressed near parallel to the (0001) basal plane; (a) Compression at peak load $P_f = 1.0$ mN, (b) propagation of planar (0001) basal crack and rotation of cleavage fragment, (c) load-displacement curve. (d-i) 3.0 μm diameter particle compressed perpendicular to the (0001) basal plane; (d) Compression at first load peak $P_f = 3.7$ mN, (e) propagation of two non-basal median cracks and a lateral (0001) basal crack, (f) lateral displacement of cleavage fragments parallel to (0001), and activation of (0001) slip bands behind indenter, (g,h) repeated generation of non-basal cracks (red arrows), basal cracks, and basal slip bands facilitate 3D shear and rotation of particle fragments (white arrows). (i) Load-displacement curve, with location of (d-h) marked.

basal slip-bands down through a single crystal NMC811 particle as it is compressed generates a characteristic pattern of multiple peaks/troughs in the load displacement curve (Figure 5(i)). The non-basal cracks are highly irregular at the nanoscale (e.g. Figure 5(h) red arrows), not exhibiting any significant $\{1\bar{1}00\}$ (prism), $\{1\bar{1}01\}$ (pyramidal), $\{01\bar{1}2\}$, or $\{10\bar{1}4\}$ fracture plane facets. The non-basal crack surfaces are also dynamically roughened by the secondary propagation of multiple parallel (0001) slip bands, which enable material to displace and rotate (parallel to (0001)) outwards from the asperity (Figure 5(g and h)). The (0001) slip bands add to the shape change of the deforming particle at the < 100 nm level, but the dominant displacements (> 100 nm) to reduce stress are achieved by the activation of basal and non-basal cracks.

Mechanical Properties of Single Crystal NMC811 Particles Cycled at C/2 and 2 C Charge/Discharge rates

At the faster cycling rates of C/2 and 2 C, the single crystal NMC811 electrode cells exhibited a ~20 mAh/g reduction in initial specific gravimetric capacity compared to the slow C/10 cycling rate, and a notable decline in capacity over cycles 50–100 to 59% (C/2) and 49% (2 C) (Figure 2(d)). After extraction from the cycled electrodes, individual SC NMC811 particles cycled at C/2 and 2 C for 100 cycles were mechanically compressed using the same in situ test parameters used for the uncycled and C/10 particles.

Figure 6 shows a comparison of mechanical properties of the uncycled single crystal NMC811 particles with particles after 100 cycles at C/10, C/2 and 2 C rates, measured from the in situ SEM compression tests. Compared to the uncycled particles, cycled SC NMC811 particles show a marked decrease in the range of yield loads P_y (mN) where cracking is first observed (Figure 6(a)), a decrease in the range of first maxima peak loads P_f (mN) (Figure 6(b)) sustained immediately prior to the first major transparticle crack propagation event, a decrease the maximum loads P_m (mN) sustained by the SC NMC811 particles (Figure 6(c)), and a decrease in contact pressures p_m (GPa) at P_f (Figure 6(d)). For the same 100 cycle testing regime, the degradation in mechanical properties increases with cycling rates C/10→C/2→2 C. For all cycling rates the cycled particles

Batteries & Supercaps

Research Article
doi.org/10.1002/batt.202400691

Chemistry
Europe

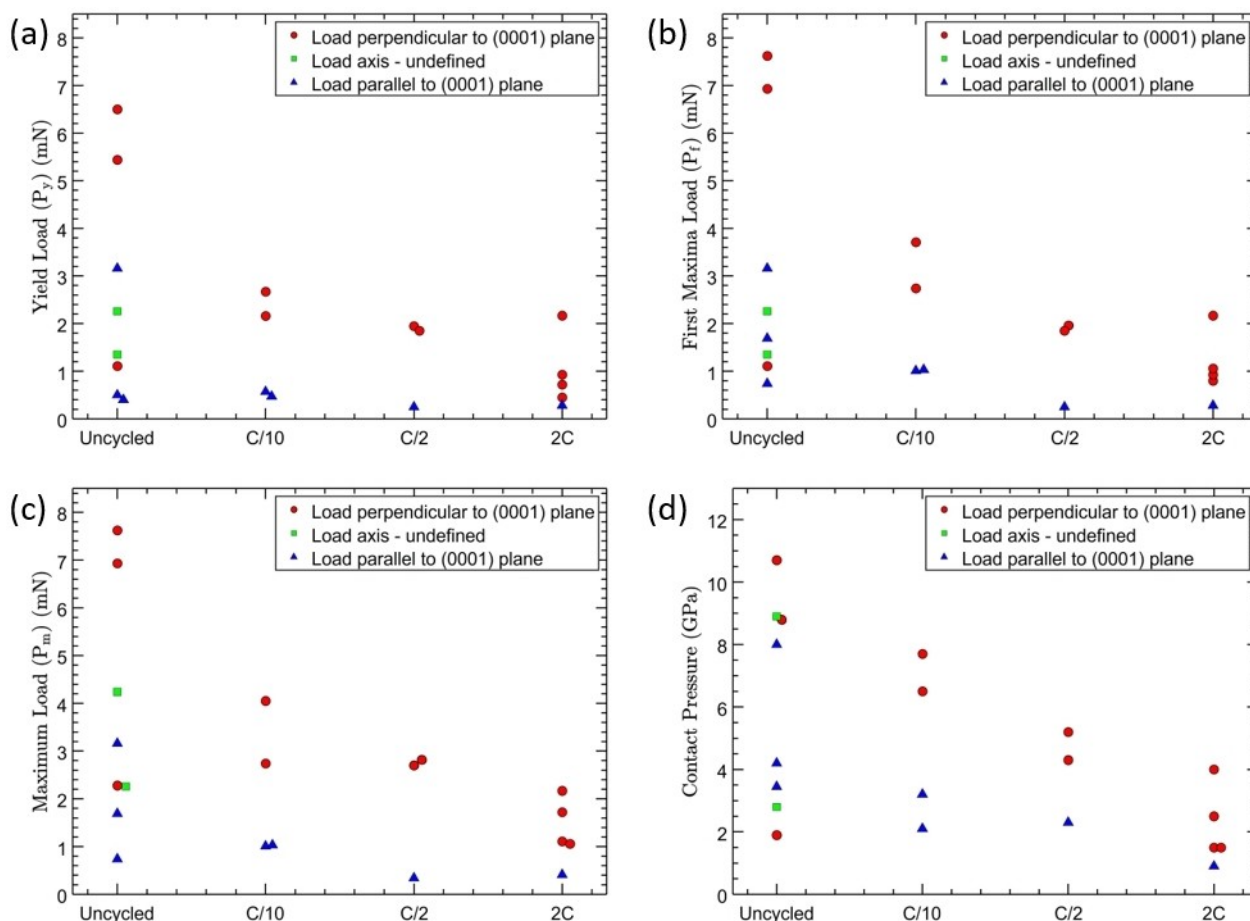European Chemical
Societies Publishing

Figure 6. Mechanical properties of single crystal NMC811 particles, from in situ compression of uncycled particles and cycled particles after 100 cycles of 3.0–4.3 V vs. Li/Li$^+$ at C/10, C/2 and 2 C. (a) Yield load at first cracking P_y (mN). (b) First maxima peak load P_f (mN) immediately prior to first major crack growth. (c) Maximum load P_m (mN) sustained by the NMC811 particle where different from (b). (d) Contact pressure p_m (GPa) at first maxima peak load P_f in (b). Particles oriented with the load axis near parallel to (0001) (blue triangles) or load axis perpendicular to (0001) (red circles) are marked.

retain the crystallographic anisotropy of mechanical strength, with cycled SC NMC811 particles strongest when compressed perpendicular to (0001)$_{R-3m}$ (Figure 6, red spots).

Single crystal NMC811 particles cycled at the faster C/2 and 2 C rates demonstrated substantial loss of mechanical strength compared to the original pristine particles, particularly when compressed near parallel to (0001) which required lower loads < 0.5 mN to initiate and propagate basal cracks through the particles (Figure 6(a–c), blue triangles). For this orientation the range of mean contact pressures p_m sustained immediately prior to rapid transparticle (0001) cracking dropped as a function of electrochemical cycling and C-rate, down from < 8 GPa for uncycled SC NMC811 particles, to < 1.0 GPa for 2 C cycled particles (Figure 6(d)), indicating significant reduction in basal fracture strength. Figure 7(a–d) shows an example of a 0.9 μm diameter NMC811 particle after 100 cycles at C/2, where compression initiates basal shear/cracking at a yield load P_y/P_f of 0.25 mN with mean contact pressure p_m of 2.3 GPa, before reaching a maximum load P_m of 0.34 mN. Basal (0001) fracture leads to transparticle cleavage and rapid generation of multiple parallel (0001) slip bands (Figure 7(b and c), red arrows) as the particle remnant still in contact with the asperity rotates away

from the loading axis like a sliding deck of cards. This rotation of the [0001] direction of the deformed NMC811 SC particle towards the load axis puts it into a mechanically harder orientation.

Figure 7(e–g) shows compression of a larger ~3 μm diameter NMC811 particle after 100 cycles at the fastest 2 C charge/discharge rate. This particular particle was moderately tabular, with a smaller satellite particle attached (RHS, Figure 7(e)). The 2 C cycled particles exhibited visible nanoscale surface roughness with < 100 nm features, due to adhered carbon and/or CEI growth (Figures 3(f), Figure 7(e and f)). The compression of the ~3 μm diameter particle initiated a basal crack at P_y/P_f = 0.28 mN (Figure 7(g)) with mean contact pressure p_m of 0.93 GPa, before reaching a maximum load of P_m = 0.41 mN. Although the loading direction in this case is through the longer dimension of the flattened particle, once the (0001) crack propagated to bisect the particle the near median (0001) fracture plane appeared planar (Figure 7(f)). Once cleaved, the remaining particle fragment still under load cracked further in the vicinity of the contact zone and rotated sideways, leaving part of the carbon/CEI surface layer adhered to the underlying substrate (Figure 7(f), yellow arrow).
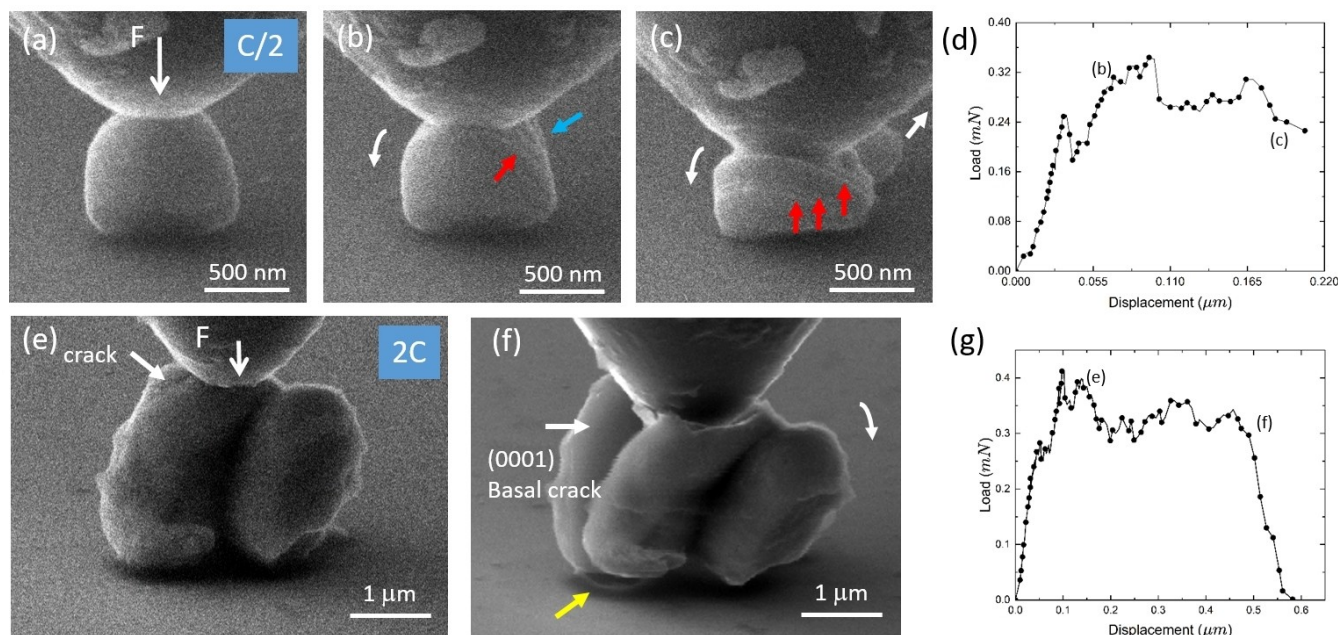
Figure 7. Compression of single crystal NMC811 particles with load axis close to the (0001) basal plane after 100 cycles of 3.0–4.3 V vs. Li/ Li$^+$ at (a-d) C/2 rate, and (e-g) 2 C rate. (a) 0.9 μm diameter single crystal NMC811 particle prior to yield, (b) (0001) basal shear (red arrow) and cracking (blue arrow), (c) particle fragmentation (white arrow, behind the tip), rotation, and growth of further (0001) slip bands (red arrows), (d) load-displacement curve for (a-c). (e) ~3 μm diameter single crystal NMC811 particle with attached satellite particle (RHS) compressed near maximum load $P_m = 0.4$ mN, (f) progressive deformation via a planar (0001) basal crack, contact zone compression, fragment rotation, and surface coating delamination (yellow arrow), (g) load-displacement curve for (e,f).

For a load axis close to [0001]$_{R-3m}$ (perpendicular to (0001)), the single crystal NMC811 particles cycled at faster C/2 and 2 C rates were markedly softer than uncycled particles compressed in the same crystallographic orientation, requiring lower loads $P_y/P_f < 2.2$ mN to initiate and propagate non-basal cracks and basal cracks through the particles, compared to $P_y/P_f < 7.6$ mN for uncycled particles (Figure 6(a and b), red circles). For this harder orientation the range of mean contact pressures p_m sustained before rapid transparticle non-basal and basal cracking dropped as a function of electrochemical cycling and C-rate, down from < 11 GPa for uncycled SC NMC811 particles, to < 8 GPa for C/10, < 5.5 GPa for C/2 and < 4 GPa for 2 C cycled particles (Figure 6(d)). This indicates a significant reduction in both non-basal and basal fracture strengths due to cycling. All C/2 and 2 C cycled single crystal NMC811 particles oriented with the load axis close to [0001] were stronger than particles cycled under the same conditions but with the load axis close to the basal plane (Figure 7), indicating that SC NMC811 crystallography still has an important role in mechanical properties after electrochemical cycling.

During compression the C/2 and 2 C cycled SC NMC811 particles compressed close to [0001]$_{R-3m}$ were found to exhibit similar deformation mechanisms to those of uncycled particles (Figure 4,[21]) or particles cycled at C/10 (Figure 5(d–i)), namely primary non-basal crack initiation, followed by secondary lateral (0001) cracks and slip bands which facilitate outwards multi-directional displacement of material to relieve contact stress. An example of SC NMC811 particle compression after C/2 rate cycling is given in Supporting information Figure S5, and a SC NMC811 particle compressed after 2 C rate cycling in Figure 8.

A short MP4 video is available for Figure 8 in Supporting Information (MP4-2).

A key change in mechanical behavior of NMC811 particles after cycling C/10→C/2→2 C was the increased ease of non-basal and (0001) basal cracking/shear, which facilitated both the rapid formation of flake-like wear fragments at significantly reduced loads/pressures, and repeated cycles of fracture down through compressed particles (Figure S5, Figure 8). Figure 8 shows a representative 1.5 μm diameter NMC811 2 C particle that undergoes repeated occurrences of the deformation sequence : primary non-basal radial/median crack growth (Figure 8(a)) → secondary lateral basal cracking and/or basal shear (Figure 8(b)) → displacement of material away from asperity generating reduction in stress (Figure 8(c)) → continued loading and repeat of this cycle (Figure 8(d and e)). Rapid multiple repeats of this sequence, which also occurred at higher loads for C/10 rate particles (Figure 5) and C/2 particles (Figure S5), results in a characteristic sawtooth shape of load curve (Figure 8(f)). The displacements of the multiple (0001) facetted lamellae generated by this mechanism are initially on parallel (0001) shear/fracture planes, but not necessarily with the same displacement vector. Overall, the displacement trajectory of the wear fragments depends first on the local stress field when the fragment first forms, and secondly on subsequent transitory stresses from surrounding wear debris and the loading asperity as compression progresses further into the particle. In situ, progressive ongoing stresses displaced partially fractured and fully-fractured wear fragments in 3-dimensions including rotation, detachment from weakly bonded satellite particles, and further fracturing/crushing of
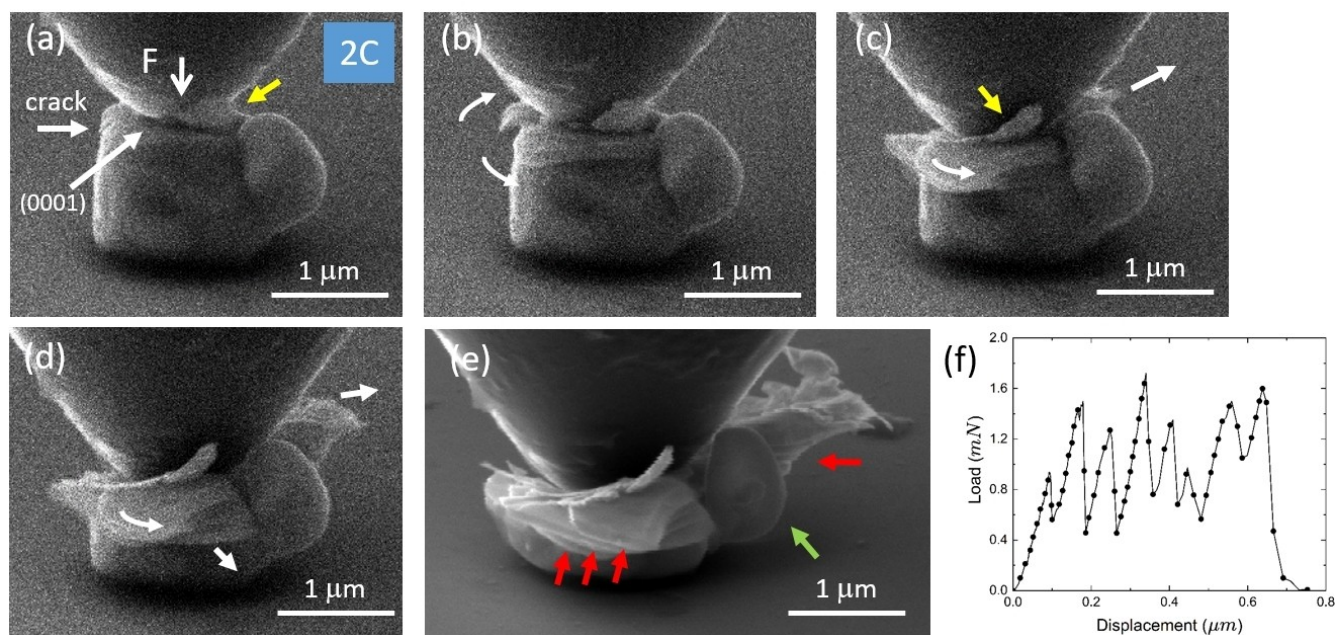
Figure 8. Compression of a 1.5 μm diameter single crystal NMC811 particle perpendicular to (0001), after 100 cycles of 3.0–4.3 V vs. Li/ Li$^+$ at 2 C. (a) 0.93 mN, non-basal radial crack initiation, and surface carbon (yellow arrow), (b) secondary lateral (0001) shear/cracking generates lamellae that displace outwards/ rotationally parallel to (0001), (c,d) progressive activation of non-basal cracking and parallel basal shear/cracking generates wear fragments with multi-directional displacements (white arrows), (e) wear debris exhibiting multiple (0001) slip bands/fracture planes (red arrows) displaced around a small satellite particle (green arrow), (f) load-displacement curve. Surface carbon agglomerates (yellow arrows) are deformed by compression.

nanoscale wear fragments particularly in the vicinity of the asperity contact zone (Figure 8(c–e)).

The adhered carbon/CEI present on NMC811 particles extracted from the electrodes cycled at 2 C rate (Figure 3(f), Figure 7(e and f)), did not appear to play any measurable role in the particle mechanical properties, with the carbon/CEI being of negligible hardness compared to the underlying ceramic. Where present, surface carbon agglomerates compressed by contacting asperities were extruded out of the contact zone (yellow arrows, Figure 8, Figure 9). It was observed that surface carbon/
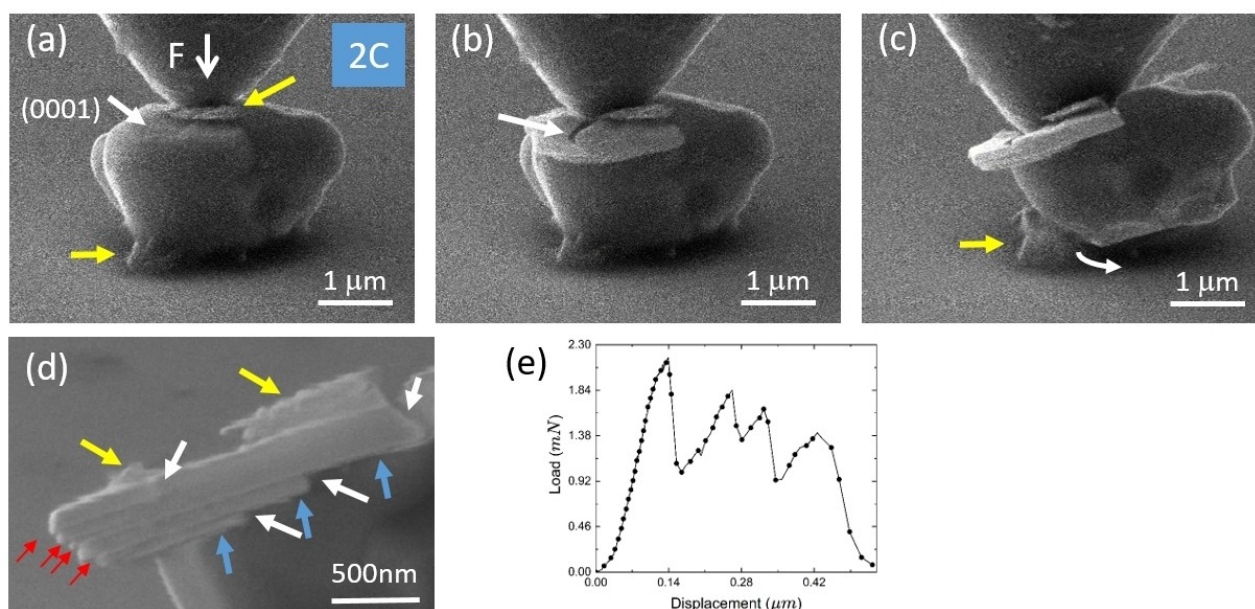

Figure 9. Compression of a 3.3 μm diameter single crystal NMC811 particle perpendicular to (0001), after 100 cycles of 3.0–4.3 V vs. Li/ Li$^+$ at 2 C. (a) 2.2 mN peak load, with attached surface carbon (yellow arrows), (b) non-basal radial crack (white arrow) and (0001) basal cracking displaces a wear fragment sideways, (c) rotation of NMC811 particle, delaminating carbon (yellow arrow), (d) close-up of wear fragment exhibiting non-basal fracture facets (white arrows), (0001) fracture facets (blue arrows), (0001) slip steps (red arrows), and surface carbon (yellow arrows), (e) load-displacement curve.

CEI layers could delaminate from cycled NMC811 particles when compressed, particularly on the underside of the particles as they rotated under load (Figure 7(f), Figure 9). Figure 9 shows a NMC811 2 C-cycled particle that initially underwent a cyclic sequence of near-surface deformation similar to the particle in Figure 8, however a local torque on the particle (due to the load axis being off-center) then initiated particle rotation and delamination of the surface carbon/CEI where it adhered to the substrate (Figure 9(c)). It is possible that thicker, softer carbon/CEI layers can act as a lubricant when trapped between NMC811 particles under torsional forces, however the graphitic nature of the original carbon black particles degrades with cycling (Figure S2b,[53,54]). Post deformation, the <500 nm thick main wear lamella (Figure 9(d)), generated by non-basal cracks (white arrows) and (0001) basal cracks (blue arrows), contains four parallel (0001) slip planes (separations 35–115 nm along [0001]) with residual slip steps of 25–70 nm in this viewing projection (red arrows). These residual slip steps are of the similar dimensions to the slip steps in the 2 C cycled particle imaged by TEM (Figure S2).

Evolution of Single Crystal NMC811 Particles with Cycling

Here, in situ mechanical testing has been used to evaluate the particle level mechanics of single crystal $LiNi_{0.8}Mn_{0.1}Co_{0.1}O_2$ (NMC811) particles, as a function of crystallographic orientation, cycling, and cycling charge/discharge rate. Key parameters that affect the mechanical strength and deformation behaviour of single crystal NMC811 particles are summarized in Figure 10.
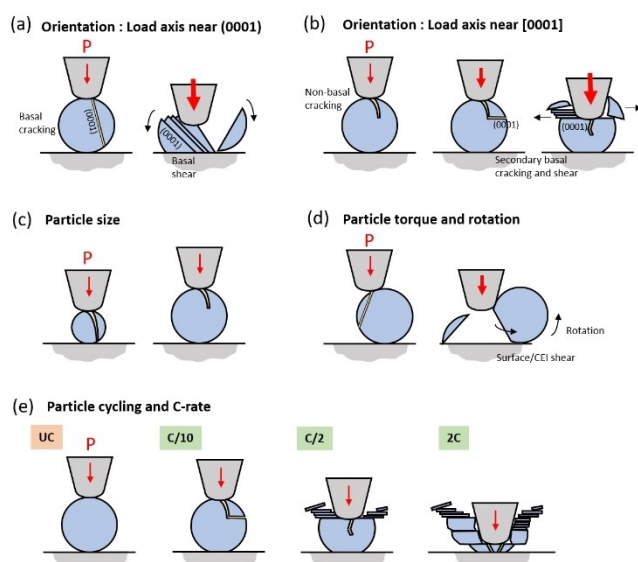

Figure 10. Mechanisms of single crystal NMC811 particle deformation during compression by a contact asperity. (a,b) Crystallographic dependent deformation sequences with increasing load for SC particles oriented with the load axis (a) near $(0001)_{R\bar{3}m}$ or (b) near $[0001]_{R\bar{3}m}$; (c) Transparticle fracture resistance of larger SC particles; (d) Surface cleavage and particle torque/rotation due to asymmetric loading directions and irregular particle shapes; (e) Softening of SC particles due to cycling, and cycling at increasing C-rate.

The commercial single crystal NMC811 particles evaluated here were 500 nm–4 µm in size with a spread of morphologies ranging from spherical to tabular. The tabular SC NMC811 particles with extended (0001) facets exhibited frequent oriented alignment of the (0001) planes/facets within the fabricated electrodes (Figure 1(a), white arrows). Such (0001) facet alignment locally increases particle packing density and will generate basal contact stresses during cycling, but still leaves the non-basal surfaces exposed to the electrolyte facilitating unhindered Li^+ ion exchange.

Under in situ compression the tabular and unfaceted SC NMC811 particles exhibited strongly anisotropic mechanical behavior consistent with that previously observed for octahedrally faceted single crystal NMC811 particles.[21] The pristine NMC811 particles are strongest when the $R\bar{3}m$ structure (0001) basal plane is oriented perpendicular to the principal load direction, sustaining the highest loads P_y/P_f up to 7.6 mN (Figures 6, 10(b)). When the principal load direction moves towards the orientation of the (0001) plane, the particles exhibit both lower yield and peak loads $P_y/P_f < 3.2$ mN (Figures 6, 10(a)). For a given orientation, larger particles generally sustained larger loads before yield and transparticle failure (Figure 10(c))[21] since the stress is distributed throughout a larger volume and transparticle cracks have further to propagate. For the SC NMC811 investigated here, the mean contact pressures sustained at maximum loads (indentation hardness) were $p_m = 2$–11 GPa (Figure 6(d)), slightly lower than the 6–14 GPa range measured for 2–4 µm diameter octahedrally facetted SC NMC811 particles,[21] and average hardness of 14 ± 3 GPa measured for ~10 µm diameter grains within polycrystalline sintered NMC811.[28]

Electrodes fabricated from the single crystal NMC811 particles were subjected to 100 cycles between 3.0–4.3 V vs. Li/Li^+ at three rates C/10, C/2 and 2 C. The cell upper cut-off voltage of 4.3 V is at or below the 4.3–4.4 V threshold typically reported for the onset of NMC811 lattice oxygen release and slip band/microcracking.[19,43,44,56] After 100 cycles, and under the same mechanical test conditions, the mechanical strength of the cycled and discharged NMC811 particles decreased compared to uncycled particles, and also decreased with increasing charge/discharge rate used C/10→C/2→2 C (Figure 6, Figure 10(e)). For all charge rates, the cycled and discharged NMC811 single crystal particles retained the crystallographic dependence of their strength from parent particles (Figure 10(a and b)). However, compared to the uncycled NMC811, after 100 cycles there is a significant drop in the load P_y required to activate the first surface cracks in the region around the asperity contact (Figure 6(a)), and a drop in the maximum loads P_f/P_m that can be sustained by the NMC811 single crystal particles (Figure 6(b and c)) indicating both surface and internal particle softening. For 100 cycles at the most aggressive 2 C cycling rate, the peak loads that could be sustained by the SC particles before major crack propagation dropped around 70 % to $P_f < 2.2$ mN, and mean contact pressures dropped around 60 % to $p_m < 4$ GPa, with the highest loads/pressures sustained by the particles compressed with the principal load direction near [0001].

After cycling, discharged single crystal NMC811 particles deformed in compression by a similar sequence of mechanisms as activated in the uncycled single crystal NMC811 particles, dominated by crystallographic dependent activation of non-basal and basal cracking, and secondary growth of basal slip bands (Figure 10(a and b)). The softening of the SC NMC811 particles with cycling is primarily due to easier activation of both basal and non-basal cracks (Figure 10(e)), equivalent to a significant drop in basal plane and non-basal plane fracture strengths. For the faster charging and harder [0001] load axis orientation the reduction of fracture strength results in the easier generation of multiple (0001)-oriented lamellae/third-body wear fragments around the asperity contact zone (Figures 8 and 9). In situ dynamical imaging reveals that both deformed zones and associated third-body wear fragments of the SC NMC811 particles are displaced in complex and time dependent 3D trajectories, including outwards from the compressing asperity, and rotationally due to local torques and/or disconnection from the parent particle (Figure 10(d and e)). Accelerated cracking facilitates large $\gg 100$ nm displacements of material, and significantly increases the total particle + fragment surface areas. Such large morphological changes are highly undesirable within an electrode, disrupting Li-ion and electronic diffusion paths and accelerating electrolyte-particle corrosion at newly exposed crack surfaces, both of which are associated with electrochemical degradation of cycled NMC particles.[6,13,14]

The occurrence of secondary basal slip, observed in situ, was particularly associated with particle shear/rotation under load after basal fracture (Figures 7, 10(a)), or lateral displacement of non-basal fracture surfaces (Figures 5, 8, 9, 10(b)). All slip bands observed, both in the uncycled[21] and cycled SC NMC811 particles, were compatible with $\mathbf{b} = \frac{a}{3} < 11\bar{2}0 > (0001)_{R\text{-}3m}$ slip systems.[37] For the conditions used there was no evidence for slip steps in the single crystal particles compatible with cross-slip of $\mathbf{b} = \frac{a}{3} < 11\bar{2}0 >$ dislocations onto prism $\{1\bar{1}00\}$ or pyramidal planes $\{1\bar{1}0n\}$ (which has been reported for sintered NMC811 cut into surface pillars by Ga-ions[33]), or the energetically unfavourable glide of dislocations with large non-basal Burgers vectors such as $\mathbf{b} = [0001]$ or $\mathbf{b} = \frac{1}{3} < 11\bar{2}3 >$. Similarly slip steps generated by non-basal glide of shorter non-basal dislocations that would generate anti-phase boundaries in the NMC811 lattice, such as $\mathbf{b} = \frac{1}{6} < 2\bar{4}23 >$[33] or $\mathbf{b} = \frac{1}{2}[0001]$ were also not observed.

Where observed, SC NMC811 particle slip band steps were nanoscale, typically in the range 10–70 nm (requiring the sequential passage of 35–250 $\mathbf{b} = \frac{a}{3} < 11\bar{2}0 >$ dislocations), and comparable with 30–50 nm basal glide steps observed in cycled NMC76.[19] The active planes of basal slip were separated by 40–120 nm along [0001] (e.g. Figures 5 and 9), indicating that it is easier to accommodate microscopic stress by activating glide of multiple dislocations on single slip planes separated by undeformed sections of crystal, rather than having to activate many more dislocation sources on adjacent/parallel slip planes. Although SEM imaging of external particle surfaces cannot always distinguish < 100 nm (0001) slip steps generated by dislocation motion (where the $R\bar{3}m$ lattice is coherent inside

the NMC811 particle except at $\mathbf{b} = \frac{a}{3} < 11\bar{2}0 >$ dislocation lines), from the early stage growth of hairline, nanowidth basal cracks (where the $R\bar{3}m$ lattice is no longer continuous along [0001] but the (0001) crack faces are still $\ll 50$ nm apart), it is clear that the dominant mechanisms for facilitating large (> 100 nm) and non-basal/3D/rotational displacements for stress relief within NMC811 single crystal particles are basal and non-basal cracking.

Electrochemical cycling causes clear degradation of the electrochemical performance of the NMC811 single crystal electrode cells, particularly at the higher C/2 and 2 C rates (Figure 2), and in situ mechanical testing identifies parallel degradation of the mechanical strengths of the individual cycled SC NMC811 particles taken from those cells (Figure 6). The decrease in particle fracture strength with cycling at faster C-rates progressively reduces the particle load/stress thresholds for cracking. For the cycling conditions used, the NMC811 single crystals in situ within the electrodes post-cycling remained intact, not exhibiting any obvious external fracture or shear/slip band damage (Figure 3), consistent with SC NMC811 cells cycled at or below 4.3 V.[16,19] The integrity of the NMC811 particles within the cycled SC electrodes examined post-mortem indicates that even with degraded mechanical properties after 100 cycles, the NMC811 single crystal particles are not reaching stresses required to induce transparticle cracking (Figure 6), either internally (e.g. stresses from chemical heterogeneity and diffusion-induced structural defects) or externally (e.g. due to electrochemically driven volume changes, Joule heating, or during electrode extraction). Stresses on particles arising from cyclic volume expansion/contraction will be enhanced at particle-particle contact points within the electrode particle assembly. The electrodes used here were uncalendered (Figure 3), which significantly reduces the density of particle-particle asperity contacts, and thus enables the particles to have translational and rotational degrees of freedom that can facilitate particle movement to reduce electrode level stresses.

The measured reduction in fracture strength of the cycled NMC811 single crystal particles is C-rate dependent (Figure 6), consistent with enhanced structural and chemical degradation of the $R\bar{3}m$ crystal structure at the faster charging and discharging rates. A range of $R\bar{3}m$ lattice degradation mechanisms in cycled NMC811 particles have been previously identified including chemical heterogeneity via lithium, oxygen and transmission metal ion loss, and cation mixing,[32,42–46] structural heterogeneity via lattice strain and internal structural defects,[5,19,30,48–52] and surface phase changes.[7,42,45,47] Here, a primary cause of the drop in fracture strength of the cycled SC NMC811 particles is residual delithiation (non-zero state of charge) after discharge, with the post-cycled discharged C/2 and 2 C electrodes exhibiting modified average a and c lattice parameters (Figure S3, supporting information) associated with Li-deficit.[7,48] The existence of $R\bar{3}m$ Li-ion vacancies reduces the attraction between adjacent Li–O basal planes and increases O–O layer repulsion,[57] increasing the c-axis lattice parameter. This lattice evolution will facilitate easier Li–O bond breaking, consistent with the observed reduction in basal and non-basal

Batteries & Supercaps

Research Article
doi.org/10.1002/batt.202400691

Chemistry Europe
European Chemical
Societies Publishing

fracture strengths (Figure 6). Related behaviour has been observed in NMC particles that have been pushed into significantly delithiated states after charging to high voltages (4.4–4.7 V),[19,30] or heating to 275 °C,[31] where the activation of non-reversible basal cracking is consistent with a drop in fracture strength. It should also be noted that persistent Li^+ vacancies in the $R\bar{3}m$ lattice (which are potentially reversible) will also facilitate secondary non-reversible processes such as cation mixing/diffusion,[32,42] oxygen migration/loss,[9,42–45] and void nucleation,[9] which will also affect mechanical behaviour.

The observed residual delithiation in the cycled SC NMC811 particles results from incomplete lithium intercalation, most likely due to both CEI growth[38–41] and surface chemical/structural degradation processes.[7,48] These processes inhibit Li^+ diffusion thereby increasing particle surface impedance,[7,11,48,58,59] and are observed here to be accelerated by C-rate. Cycling with higher C-rates means using higher local ion and electron current densities, which modify the diffusion of Li-ions, electrons, and lattice ions/atoms in both electrodes and electrolyte due to enhanced Joule heating, increased ion/electron/atom scattering, and increased defect generation (e.g. lattice disorder), thereby altering the kinetics of electrolyte-electrode reactions, CEI growth and NMC811 lattice degradation processes. Here, the SC NMC811 particles cycled at most aggressive 2 C-rate exhibited both significant CEI growth, and accelerated surface degradation in the form of limited cubic spinel ordering at the crystalline surface of the SC NMC811 particles (Figure S2, supporting information) due to Li and oxygen loss,[42,43] although no shift from trigonal to cubic mechanical behaviour, or rock salt formation[7,42,47] was observed in this study.

For the electrochemical conditions used, cycled SC NMC811 particles exhibited a significant drop in near-surface mechanical strength (< 200 nm deep) compared to the uncycled particles, including reductions in the yield load P_y for first crack initiation (Figure 6(a)), and the peak load P_f and contact pressure p_m sustainable before the first major crack propagation (Figure 6(b and d)). For cycled NMC811 particles compressed down the strongest $[0001]_{R-3m}$ load direction, a higher load P_m, where $P_m > P_f$, was frequently required to activate cracking events deeper into the particles (Figures 5(d–i), Figure 8, Figure S5). However in all cases the inner strength of the particles was lower than for uncycled particles, with the maximum load P_m sustained by the cycled NMC811 particles systematically decreasing with the cycling rate used C/10→C/2→2 C (Figure 6(c)). A depth-dependant load to activate major crack propagation events is consistent with a higher degree of $R\bar{3}m$ lattice degradation at the particle surfaces, particularly induced by higher C-rates. Similar behaviour of easier crack propagation in near-surface volumes can also be associated, to a lesser degree, with compression of hemi-spherical/irregular particle surfaces (e.g. Figure 5), where geometrically the compressed volume increases significantly with depth. Additionally, particles compressed down the softer orientation with the load axis initially close to $(0001)_{R-3m}$ can become harder during a compression event by rotating $[0001]_{R-3m}$ towards the load axis (Figure 7). However regardless of geometric and crystallographic differ-

ences, for the same number of electrochemical cycles the mechanical strength of the cycled SC NMC811 particles degrades faster at higher C-rates (Figure 6).

In this study, the faster C/2 and 2 C charge/discharge rates led to accelerated growth of an amorphous cathode electrolyte interphase (CEI) on the surface of the SC NMC811 particles (Figures 3, 7, Figure S2), which is known to contribute to the degradation of the electrochemical performance of half-cells.[38–41] On the NMC811 particles, growth of the CEI layer can act as a trap for diffusing Li, O, Ni, Mn and Co ions,[38,40] leaving the NMC811 particles irreversibly chemically denuded and structurally defective, as well as hindering Li-ion and electron diffusion in and out of the particles increasing surface impedance.[11,58,59] Here the loss of lattice atoms associated with the transition of the NMC811 $R\bar{3}m$ lattice to surface spinel at 2 C cycling rate (Figure S2), likely contributes to the accelerated CEI growth as well as particle surface softening. Significant amorphisation/swelling of the conductive carbon nanoparticles also occurred (Figure 3), which increased significantly with C-rate C/10→C/2→2 C. Carbon black can degrade by carbon-electrolyte reactions, absorption of Li-ions,[53,54] and also trap metal ions that have escaped into the electrolyte from NMC811 degradation processes.[38] In comparison with the original highly conductive graphitic carbon black, the degraded amorphous carbon prevalent at the faster charge rates will be less conductive, hindering electron diffusion required for redox processes and increasing electrode resistance.[53,54] The flexibility, adhesiveness and conductivity of the carbon additive are important factors in maintaining good electron conduction paths between the active NMC811 particles and current collector during cyclic electrode stresses. In situ mechanical testing here shows that the CEI/surface carbon layer was flexible and soft compared to the NMC811 single crystals, and was easily deformed (e.g. Figures 7 and 8). However, in some in situ compression tests the degraded CEI/carbon surface layer delaminated from the SC NMC811 particles during particle movement/rotation (Figures 7(f), Figure 9(c)), which within an electrode environment would sever the electronic path and leave freshly exposed SC surfaces vulnerable to electrolyte attack.

Conclusions

In this study the evolution of the mechanical properties of single crystal $LiNi_{0.8}Mn_{0.1}Co_{0.1}O_2$ (NMC811) particles with electrochemical cycling has been evaluated in detail at the individual particle level. In situ SEM mechanical compression has been successfully employed to evaluate both the quantitative fracture strengths of individual cycled SC NMC811 particles, and to determine the dynamical deformation mechanisms that occur after different cycling conditions.

For the cycling regimes and cell architecture used, electrochemical cycling at the faster C/2 and 2 C rates caused accelerated degradation of the electrochemical performance of the SC NMC811 cathode cells compared to C/10, and in situ mechanical testing identifies parallel degradation of the

Batteries & Supercaps

Research Article
doi.org/10.1002/batt.202400691

Chemistry Europe
European Chemical
Societies Publishing

mechanical properties of the SC particles. After 100 cycles individual SC NMC811 particles demonstrated a systematic loss of mechanical strength as a function of increasing C-rate C/10→2 C used. For the most aggressive 2 C cycling rate, the peak loads that could be sustained by the 500 nm–4 μm sized SC particles before major crack propagation dropped around 70% to $P_f < 2.2$ mN, and mean contact pressures dropped around 60% to $p_m < 4$ GPa. The deformation mechanisms of the cycled SC NMC811 remained dominated by the orientation of the trigonal $R\bar{3}m$ crystal lattice with respect to the principal load direction, with the highest loads/pressures sustained by the particles compressed with the principal load direction near [0001] before the activation of non-basal cracking and secondary basal cracking and shear. In contrast, cycled NMC811 particles with the load axis close to (0001) are weaker, with lower load activation of basal fracture and slip. As for pristine particles, slip bands in deformed cycled SC particles were only consistent with $\mathbf{b} = \frac{a}{3} < 11\bar{2}0 > (0001)$ slip systems, indicative of severely restricted dislocation driven plasticity.

The mechanical degradation of the cycled SC NMC811 particles is associated with a decrease in both non-basal and basal plane fracture strengths, which progressively lower the load and pressure thresholds required to propagate cracks through the cycled particles in all crystallographic orientations. In situ mechanical testing shows that once local fracture thresholds are reached, the most mechanically degraded SC NMC811 particles exhibit an increased density/frequency of basal and non-basal fracture and basal slip band generation, particularly near the particle surfaces where lattice degradation processes are accelerated. Increased particle deformation/fragmentation, and associated increases in particle + fragment surface areas, are highly undesirable within electrodes, disrupting Li-ion and electronic diffusion paths and accelerating electrolyte-particle corrosion at newly exposed crack surfaces, both of which are associated with electrochemical degradation of cycled NMC particles. In this study, the cycled SC NMC811 particles in uncalendered electrodes cycled to 4.3 V vs. Li/Li$^+$ did not exhibit any significant external morphology changes in-situ within the electrodes. Thus although the fast electrochemical cycling regimes are systematically reducing the SC NMC811 particles resistance to stress, the decreasing threshold for fracture was not reached within the cycle regimes and electrode architecture used. This clearly demonstrates that visual inspection of external particle integrity is not a satisfactory indicator of state of mechanical health of the NMC811 particles.

This evaluation of the mechanical properties of cycled SC NMC811 reveals that key cathode design criteria to reduce the rate of particle mechanical degradation and avoid activation of detrimental cracking, should include management/reduction of fast-charging cycling regimes, and optimization of SC particle architecture (shape, size, packing, oriented alignment and texture) to reduce asperity contacts and reduce electrode stresses particularly along the weaker $(0001)_{R-3m}$ basal planes. Reduction of the density of particle-particle asperity contacts, and maintenance of individual particle mobility to reduce asperity stress, can be facilitated by avoiding aggressive calendering.

Experimental Methods

Materials

Here the mechanical properties of commercial single crystal NMC811 powder (Li-Fun Technology, China) with composition LiNi$_{0.8}$Mn$_{0.1}$Co$_{0.1}$O$_2$ have been investigated. The microstructures of the NMC811 particles, both as received and after electrochemical cycling, were characterized by Scanning Electron Microscopy (SEM), Transmission Electron Microscopy (TEM) and X-ray Diffraction (XRD). All specimen storage, cell preparation and sample preparation was carried out inside an Ar filled glovebox.

Electrode and Coin Cell Preparation

Single crystal (SC) electrodes were synthesized by first preparing a slurry using 90 wt% SC NMC811 cathode particles as an active material, 5 wt% polyvinylidene fluoride (PVDF; MTI) as a binder, 5 wt% Super C65 carbon black (C-Nergy TIMCAL) as a conductive agent, and N-methyl-2-pyrrolidone, NMP, (Sigma-Aldrich) as solvent, using an orbital mixer (Thinky). This slurry was tape-cast onto the carbon-coated side of aluminium foil using a 200 μm thickness doctor blade, kept at 80 °C for 45 minutes to let the NMP dry off, and then placed in a vacuum oven at 80 °C for 24 hrs. Electrode discs with 12 mm diameter were punched out of the dried tape-cast electrode sheet. No calendering was carried out to avoid mechanical damage of the NMC particles.

Half-cells were fabricated using CR2016 stainless steel coin cells (Cambridge Energy Solutions), using 0.5 mm thick stainless disc spacers, an 8 mm diameter Li disc anode (Sigma Aldrich), a Celgard 2325 polypropylene−polyethylene−polypropylene trilayer separator soaked in 100 μL of lithium hexafluorophosphate (LiPF$_6$) in a 50/50 volume ratio of ethylene carbonate (EC) and dimethyl carbonate (DMC) as an electrolyte, and the prepared SC NCM811 electrode disc cathodes. The coin cells were crimped together in Ar filled glove box (mBRAUN).

Electrochemical Testing

The prepared coin cells were cycled using a Maccor galvanostat. Prior to cycling, the cells were left to rest for 12 hours. For each cell, two formation cycles were first carried out at a C/20 charge-discharge rate between 3.0 V vs. Li/Li$^+$ and 4.3 V vs. Li/Li$^+$. Subsequently, 100 complete cycles were performed galvanostatically (constant current) between 3.0–4.3 V vs. Li/Li$^+$, with 1 hour rest between each cycle. Cells were cycled at one of three different charge-discharge rates, i.e. slow C/10, intermediate C/2, or fast 2 C. The theoretical specific capacity of NMC811, which is 200 mAhg^{-1}, was used to calculate the C-rate. After each galvanostatic charge the coin cells were potentiostatically held at 4.3 V vs. Li/Li$^+$ for 30 minutes before discharge, and cycling was stopped after the 100th discharge cycle at 3.0 V vs. Li/Li$^+$. Two coin cells were cycled at each C-rate and exhibited similar electrochemical behaviour.

Particle Preparation for Mechanical Testing

Post electrochemical cycling the coin cells were disassembled in an Ar-filled glove box. The cells were de-crimped, and the discharged electrodes rinsed with dimethyl carbonate (DMC) (Sigma Aldrich) to

Batteries & Supercaps

Research Article
doi.org/10.1002/batt.202400691

Chemistry
Europe

European Chemical
Societies Publishing

remove the electrolyte and then dried. The cycled NMC811 particles were extracted from the cathodes by soaking in N-methyl 2-pyrrolidone (NMP) (Sigma Aldrich) for 1 hour at room temperature to dissolve the binder. After soaking and ultrasonication, the cycled NMC811 particle suspensions were drop cast onto Si wafers, and then mounted on SEM stubs for imaging and mechanical testing. Pristine NMC811 particles were prepared for mechanical testing by dispersing in ethanol and drop casting onto Si wafers. TEM samples of the pristine and 2 C cycled NMC811 particles were prepared by drop casting particle suspensions onto holey carbon grids. SEM and TEM samples were briefly exposed to air ($<$5 min) during transfer into the SEM and TEM microscopes. Secondary electron (SE) SEM imaging was carried at 10 kV (FEI Nova 450). TEM imaging and selected area electron diffraction (SAED) were carried out at 200 kV (JEOL F200 TEM) and recorded with a Gatan One View camera.

In situ SEM Mechanical Testing

Mechanical testing of the pristine and cycled NMC811 particles was carried out using an in situ SEM microindenter (Alemnis AG) mounted in an SEM (FEI Nova 450) using the methodology previously developed.[21,26] Individual particles were compressed by a diamond conospherical tip (Synton MDP; Poisson's ratio – 0.07, Young's modulus 1140 GPa) with a 1 μm radius of curvature. Using in situ secondary electron (SE) imaging with a 10 kV electron beam, individual particles were chosen and moved via a translation stage to be directly under the diamond tip, with a contact point away from facet edges. A representative range of NMC811 single crystal particles with both irregular/polyhedral and tabular morphologies was tested to investigate the influence of particle shape, size and orientation on mechanical properties. The particles were indented under a ramped load control at 0.3 mNs^{-1}, measuring tip displacement during loading. Each load curve was corrected for load drift, and the displacement corrected to zero at zero load (Alemnis AMMDA software).

Mechanical property parameters extracted from the load-displacement curves included (i) the load at yield P_y (mN) where cracking is first observed, (ii) the first maxima peak load P_f (mN) which is the critical load occurring immediately prior to the first major transparticle crack propagation event, and (iii) the maximum load P_m (mN) sustained by the SC NMC811 particle during the test. For rapid basal crack propagation though small particles and loading parallel to (0001) often $P_y = P_f$, since the crack initiation and rapid propagation are concurrent. For uncycled SC NMC811 tests, where there is no enhanced surface degradation, typically $P_f = P_m$ (Figure 6).

The mean contact pressure p_m exerted on a given particle at the critical load P_f, which leads to the first major propagation of cracking through the loaded SC NMC811 particle, was estimated by calculating the tip contact area using the indenter-NMC particle contact radius measured directly from the in situ imaging immediately prior to fracture. This contact pressure p_m is equivalent to indentation hardness, and gives a direct measure of the stress required to fracture the SC NMC811 particles.

Conflict of Interests

The authors declare no conflict of interest.

Data Availability Statement

The data that support the findings of this study are available in the supplementary material of this article.

[1] J. U. Choi, N. Voronina, Y. K. Sun, S. T. Myung, *Adv. Energy Mater.* **2020**, *10*, DOI 10.1002/aenm.202002027.

[2] S. G. Booth, A. J. Nedoma, N. N. Anthonisamy, P. J. Baker, R. Boston, H. Bronstein, S. J. Clarke, E. J. Cussen, V. Daramalla, M. De Volder, S. E. Dutton, V. Falkowski, N. A. Fleck, H. S. Geddes, N. Gollapally, A. L. Goodwin, J. M. Griffin, A. R. Haworth, M. A. Hayward, S. Hull, B. J. Inkson, B. J. Johnston, Z. Lu, J. L. MacManus-Driscoll, X. Martínez De Irujo Labalde, I. McClelland, K. McCombie, B. Murdock, D. Nayak, S. Park, G. E. Pérez, C. J. Pickard, L. F. J. Piper, H. Y. Playford, S. Price, D. O. Scanlon, J. C. Stallard, N. Tapia-Ruiz, A. R. West, L. Wheatcroft, M. Wilson, L. Zhang, X. Zhi, B. Zhu, S. A. Cussen, *APL Mater.* **2021**, *9*, DOI 10.1063/5.0051092.

[3] K. Ishidzu, Y. Oka, T. Nakamura, *Solid State Ion* **2016**, *288*, 176–179.

[4] S. Xia, L. Mu, Z. Xu, J. Wang, C. Wei, L. Liu, P. Pianetta, K. Zhao, X. Yu, F. Lin, Y. Liu, *Nano Energy* **2018**, *53*, 753–762.

[5] A. O. Kondrakov, A. Schmidt, J. Xu, H. Geßwein, R. Mönig, P. Hartmann, H. Sommer, T. Brezesinski, J. Janek, *J. Phys. Chem. C* **2017**, *121*, 3286–3294.

[6] H. H. Ryu, K. J. Park, C. S. Yoon, Y. K. Sun, *Chem. Mater.* **2018**, *30*, 1155–1163.

[7] S. Schweidler, L. De Biasi, G. Garcia, A. Mazilkin, P. Hartmann, T. Brezesinski, J. Janek, *ACS Appl. Energy Mater.* **2019**, *2*, 7375–7384.

[8] L. Wheatcroft, A. Bird, J. C. Stallard, R. L. Mitchell, S. G. Booth, A. J. Nedoma, M. F. L. De Volder, S. A. Cussen, N. A. Fleck, B. J. Inkson, *Batter. Supercaps* **2023**, *6*, DOI 10.1002/batt.202300032.

[9] L. Mu, R. Lin, R. Xu, L. Han, S. Xia, D. Sokaras, J. D. Steiner, T. C. Weng, D. Nordlund, M. M. Doeff, Y. Liu, K. Zhao, H. L. Xin, F. Lin, *Nano Lett.* **2018**, *18*, 3241–3249.

[10] T. M. M. Heenan, A. Wade, C. Tan, J. E. Parker, D. Matras, A. S. Leach, J. B. Robinson, A. Llewellyn, A. Dimitrijevic, R. Jervis, P. D. Quinn, D. J. L. Brett, P. R. Shearing, *Adv. Energy Mater.* **2020**, *10*, DOI 10.1002/aenm.202002655.

[11] W. M. Dose, J. K. Morzy, A. Mahadevegowda, C. Ducati, C. P. Grey, M. F. L. De Volder, *J. Mater. Chem. A Mater.* **2021**, *9*, 23582–23596.

[12] K. Raju, L. Wheatcroft, M. C. Lai, A. Mahadevegowda, L. F. J. Piper, C. Ducati, B. Inkson, M. De Volder, *J. Electrochem. Soc.* **2024**, DOI 10.1149/1945-7111/ad6378.

[13] H. H. Sun, H. H. Ryu, U. H. Kim, J. A. Weeks, A. Heller, Y. K. Sun, C. B. Mullins, *ACS Energy Lett.* **2020**, *5*, 1136–1146.

[14] G. Qian, Y. Zhang, L. Li, R. Zhang, J. Xu, Z. Cheng, S. Xie, H. Wang, Q. Rao, Y. He, Y. Shen, L. Chen, M. Tang, Z. F. Ma, *Energy Storage Mater.* **2020**, *27*, 140–149.

[15] F. Li, L. Kong, Y. Sun, Y. Jin, P. Hou, *J. Mater. Chem. A Mater.* **2018**, *6*, 12344–12352.

[16] Y. Liu, J. Harlow, J. Dahn, *J. Electrochem. Soc.* **2020**, *167*, 020512.

[17] J. Langdon, A. Manthiram, *Energy Storage Mater.* **2021**, *37*, 143–160.

Batteries & Supercaps

Research Article
doi.org/10.1002/batt.202400691

Chemistry Europe
European Chemical
Societies Publishing

[18] J. Zhu, G. Chen, *J. Mater. Chem. A Mater.* **2019**, *7*, 5463–5474.

[19] Y. Bi, J. Tao, Y. Wu, L. Li, Y. Xu, E. Hu, B. Wu, J. Hu, C. Wang, J. G. Zhang, Y. Qi, J. Xiao, *Science (1979)* **2020**, *370*, 1313–1318.

[20] Y. Bi, Y. Xu, R. Yi, D. Liu, P. Zuo, J. Hu, Q. Li, J. Wu, C. Wang, S. Tan, E. Hu, J. Li, R. O'Toole, L. Luo, X. Hao, S. Venkatachalam, J. Rijssenbeek, J. Xiao, *Energy Storage Mater.* **2023**, *62*, DOI 10.1016/j.ensm.2023.102947.

[21] L. Wheatcroft, A. Bird, N. Gollapally, S. G. Booth, S. A. Cussen, B. J. Inkson, *Batter. Supercaps* **2024**, DOI 10.1002/batt.202400077.

[22] H. H. Ryu, B. Namkoong, J. H. Kim, I. Belharouak, C. S. Yoon, Y. K. Sun, *ACS Energy Lett.* **2021**, *6*, 2726–2734.

[23] I. A. Moiseev, A. A. Savina, A. D. Pavlova, T. A. Abakumova, V. S. Gorshkov, E. M. Pazhetnov, A. M. Abakumov, *Energy Adv.* **2022**, *10*, 677–681.

[24] D. R. Diercks, M. Musselman, A. Morgenstern, T. Wilson, M. Kumar, K. Smith, M. Kawase, B. P. Gorman, M. Eberhart, C. E. Packard, *J. Electrochem. Soc.* **2014**, *161*, F3039–F3045.

[25] D. Dang, Y. Wang, Y.-T. Cheng, *J. Electrochem. Soc.* **2019**, *166*, A2749–A2751.

[26] L. Wheatcroft, A. Bird, J. C. Stallard, R. L. Mitchell, S. G. Booth, A. J. Nedoma, M. F. L. De Volder, S. A. Cussen, N. A. Fleck, B. J. Inkson, *Batter. Supercaps* **2023**, *6*, DOI 10.1002/batt.202300032.

[27] S. Maeng, Y. Chung, S. Min, Y. Shin, *J. Power Sources* **2020**, *448*, DOI 10.1016/j.jpowsour.2019.227395.

[28] N. Sharma, D. Meng, X. Wu, L. S. de Vasconcelos, L. Li, K. Zhao, *Extreme Mech. Lett.* **2023**, *58*, DOI 10.1016/j.eml.2022.101920.

[29] J. C. Stallard, S. Vema, D. S. Hall, A. R. Dennis, M. E. Penrod, C. P. Grey, V. S. Deshpande, N. A. Fleck, *J. Electrochem. Soc.* **2022**, *169*, 040511.

[30] P. Yan, J. Zheng, M. Gu, J. Xiao, J. G. Zhang, C. M. Wang, *Nat. Commun.* **2017**, *8*, DOI 10.1038/ncomms14101.

[31] P. Yan, J. Zheng, T. Chen, L. Luo, Y. Jiang, K. Wang, M. Sui, J. G. Zhang, S. Zhang, C. Wang, *Nat. Commun.* **2018**, *9*, DOI 10.1038/s41467-018-04862-w.

[32] Q. Lin, W. Guan, J. Zhou, J. Meng, W. Huang, T. Chen, Q. Gao, X. Wei, Y. Zeng, J. Li, Z. Zhang, *Nano Energy* **2020**, *76*, DOI 10.1016/j.nanoen.2020.105021.

[33] S. Wang, Z. Shen, A. Omirkhan, O. Gavalda-Diaz, M. P. Ryan, F. Giuliani, *J. Eur. Ceram. Soc.* **2023**, *43*, 7553–7560.

[34] F. Zhang, S. Lou, S. Li, Z. Yu, Q. Liu, A. Dai, C. Cao, M. F. Toney, M. Ge, X. Xiao, W. K. Lee, Y. Yao, J. Deng, T. Liu, Y. Tang, G. Yin, J. Lu, D. Su, J. Wang, *Nat. Commun.* **2020**, *11*, DOI 10.1038/s41467-020-16824-2.

[35] L. Wu, J. Zhang, *J. Appl. Phys.* **2015**, *118*, DOI 10.1063/1.4937409.

[36] M. Sadowski, L. Koch, K. Albe, S. Sicolo, *Chem. Mater.* **2022**, DOI 10.1021/acs.chemmater.2c03069.

[37] H. Gabrisch, R. Yazami, B. Fultz, *Electrochem. Solid-State Lett.* **2002**, *5*, DOI 10.1149/1.1472257.

[38] W. Li, A. Dolocan, P. Oh, H. Celio, S. Park, J. Cho, A. Manthiram, *Nat. Commun.* **2017**, *8*, DOI 10.1038/ncomms14589.

[39] Y. Wu, X. Liu, L. Wang, X. Feng, D. Ren, Y. Li, X. Rui, Y. Wang, X. Han, G. L. Xu, H. Wang, L. Lu, X. He, K. Amine, M. Ouyang, *Energy Storage Mater.* **2021**, *37*, 77–86.

[40] T. Kim, *Mater. Today Sustainability* **2023**, *21*, DOI 10.1016/j.mtsust.2023.100326.

[41] R. C. McNulty, E. Hampson, L. N. Cutler, C. P. Grey, W. M. Dose, L. R. Johnson, *J Mater. Chem. A Mater.* **2023**, *11*, 18302–18312.

[42] K. W. Nam, S. M. Bak, E. Hu, X. Yu, Y. Zhou, X. Wang, L. Wu, Y. Zhu, K. Y. Chung, X. Q. Yang, *Adv. Funct. Mater.* **2013**, *23*, 1047–1063.

[43] R. Jung, M. Metzger, F. Maglia, C. Stinner, H. A. Gasteiger, *J. Electrochem. Soc.* **2017**, *164*, A1361–A1377.

[44] D. Streich, C. Erk, A. Guéguen, P. Müller, F. F. Chesneau, E. J. Berg, *J. Phys. Chem. C* **2017**, *121*, 13481–13486.

[45] J. Wandt, A. T. S. Freiberg, A. Ogrodnik, H. A. Gasteiger, *Mater. Today* **2018**, *21*, 825–833.

[46] B. G. Chae, S. Y. Park, J. H. Song, E. Lee, W. S. Jeon, *Nat. Commun.* **2021**, *12*, DOI 10.1038/s41467-021-24120-w.

[47] F. Lin, I. M. Markus, D. Nordlund, T. C. Weng, M. D. Asta, H. L. Xin, M. M. Doeff, *Nat. Commun.* **2014**, *5*, 3529.

[48] F. Friedrich, B. Strehle, A. T. S. Freiberg, K. Kleiner, S. J. Day, C. Erk, M. Piana, H. A. Gasteiger, *J. Electrochem. Soc.* **2019**, *166*, A3760–A3774.

[49] W. Li, H. Y. Asl, Q. Xie, A. Manthiram, *J. Am. Chem. Soc.* **2019**, *141*, 5097–5101.

[50] X. H. Meng, T. Lin, H. Mao, J. L. Shi, H. Sheng, Y. G. Zou, M. Fan, K. Jiang, R. J. Xiao, D. Xiao, L. Gu, L. J. Wan, Y. G. Guo, *J. Am. Chem. Soc.* **2022**, *144*, 11338–11347.

[51] S. Ahmed, A. Pokle, M. Bianchini, S. Schweidler, A. Beyer, T. Brezesinski, J. Janek, K. Volz, *Matter* **2021**, *4*, 3953–3966.

[52] S. Li, Z. Yao, J. Zheng, M. Fu, J. Cen, S. Hwang, H. Jin, A. Orlov, L. Gu, S. Wang, Z. Chen, D. Su, *Angew. Chem. Int. Ed.* **2020**, *59*, 22092–22099.

[53] J. Syzdek, M. Marcinek, R. Kostecki, *J. Power Sources* **2014**, *245*, 739–744.

[54] R. Younesi, A. S. Christiansen, R. Scipioni, D.-T. Ngo, S. B. Simonsen, K. Edström, J. Hjelm, P. Norby, *J. Electrochem. Soc.* **2015**, *162*, A1289–A1296.

[55] S. M. Bak, E. Hu, Y. Zhou, X. Yu, S. D. Senanayake, S. J. Cho, K. B. Kim, K. Y. Chung, X. Q. Yang, K. W. Nam, *ACS Appl. Mater. Interfaces* **2014**, *6*, 22594–22601.

[56] W. M. Dose, W. Li, I. Temprano, C. A. O'Keefe, B. L. Mehdi, M. F. L. De Volder, C. P. Grey, *ACS Energy Lett.* **2022**, *7*, 3524–3530.

[57] R. Xu, H. Sun, L. S. de Vasconcelos, K. Zhao, *J. Electrochem. Soc.* **2017**, *164*, A3333–A3341.

[58] Y. Qian, P. Niehoff, M. Börner, M. Grützke, X. Mönnighoff, P. Behrends, S. Nowak, M. Winter, F. M. Schappacher, *J. Power Sources* **2016**, *329*, 31–40.

[59] S. Liu, J. Su, J. Zhao, X. Chen, C. Zhang, T. Huang, J. Wu, A. Yu, *J. Power Sources* **2018**, *393*, 92–98.